Elucidating the origin of heterogeneous anomalous diffusion in the cytoplasm of mammalian cells

Adal Sabri[1], Xinran Xu[2], Diego Krapf[2,3,*], and Matthias Weiss[1,*]

[1] *Experimental Physics I, University of Bayreuth, D-95440 Bayreuth, Germany*
[2] *Dept. of Electrical and Computer Engineering, and* [3] *School of Biomedical Engineering, Colorado State University, Fort Collins, CO 80523, USA*

Diffusion of tracer particles in the cytoplasm of mammalian cells is often anomalous with a marked heterogeneity even within individual particle trajectories. Despite considerable efforts, the mechanisms behind these observations have remained largely elusive. We performed extensive single-particle tracking experiments on quantum dots in the cytoplasm of live mammalian cells (unperturbed or after disrupting the cytoskeleton). Analyses of the trajectories reveal a strong, microtubule-dependent subdiffusion with antipersistent increments and a substantial heterogeneity. Comparison to simulations highlight that the motion can be fully described as an intermittent fractional Brownian motion, alternating between two states of different mobility. Our data indicate transient associations with the endoplasmic reticulum (ER) network to be key for the low-mobility state. In addition, the ER couples the particle motion indirectly to active, cytoskeleton-based transport processes.

The cytoplasm of mammalian cells is a complex aqueous environment, crowded with large amounts of macromolecules [1, 2] and a multitude of membrane-enveloped organelles of largely varying sizes. Diffusion of supposedly inert tracer particles in the cytoplasm of living cells has frequently been reported to be anomalous with a sublinear scaling of the mean square displacement (MSD), $\langle r^2(\tau)\rangle \sim t^\alpha$ ($\alpha < 1$) on spatio-temporal scales below a few micrometers and several seconds [3–5]. The emergence of subdiffusive motion appears in many cases to be consistent with a stochastic process of the fractional Brownian motion (FBM) type [6–8], i.e. a self-similar Gaussian process with stationary increments whose features are determined by the Hurst coefficient $H = \alpha/2$ [9]. FBM dynamics is subdiffusive for $0 < H < 1/2$ and trajectories are characterized by antipersistent, i.e. anticorrelated, increments. A plausible interpretation for such antipersistent memory effects is a viscoelastic environment [10–15] with a complex shear modulus that scales as $G(\omega) \sim \omega^\alpha$, where the elastic and the viscous parts are responsible for the FBM memory and for energy dissipation, respectively.

Subdiffusion has long been recognized to emerge in solutions crowded with macromolecules, with an anomaly exponent α that decreases with crowder concentration [16, 17]. However, the value of α is often observed to be considerably lower in the cytoplasm than in similarly crowded artificially fluids, e.g. $\alpha \approx 0.6$ [10, 18] versus $\alpha \approx 0.8$ [11, 14]. Therefore, it is currently understood that subdiffusion in the cytoplasm may not be caused solely by macromolecular crowding but also relies on additional mechanisms. As of yet, no general agreement exists for a physical model that can reliably describe cytoplasmic subdiffusion in detail. Further, subdiffusion is not universal but depends on tracer size, e.g. for particles in reconstituted entangled actin filament networks, where α can be continuously tuned between zero and unity as a function of particle radius and average mesh size [19]. Beyond such caging effects, it has also been proposed that non-inert crowders may strongly alter the dynamics of cytoplasmic particles [20, 21]. Extensive Monte Carlo simulations have supported this hypothesis [22]. More recently, also experimental support has been obtained via single-particle tracking (SPT) on surface-modified tracer particles in the cytoplasm of HeLa cells: The emergence of subdiffusion and the value of α was shown to depend both on particle size and non-specific interactions to the cytoplasmic interior [18]. Yet, the identity of the cytoplasmic binding partners that enforce the emergence of subdiffusive motion has remained elusive. Potential candidates include the cytoskeleton and organelles, e.g. the endoplasmic reticulum (ER) network that pervades the cytoplasm [23].

Further, local variations in complex media are noticeable in the motion of particles therein: (Sub)diffusion in cellular fluids has been observed to be heterogeneous even within individual trajectories [24–26], suggesting heterogeneous diffusion processes [27] or spatiotemporal variations of transport coefficients [28–30]. Despite the elegance of these theoretical models, it remains an open question how a distribution of apparent diffusivities emerges in the first place. A potential source might be the ambient active noise in the cytoplasm, i.e. the chemically induced rattling and shaking of the environment due to the non-equilibrium action of molecular motors and cytoskeletal filaments. In fact, breaking down cytoskeletal filaments alters the subdiffusive motion of organelle structures in mammalian cells [31, 32] and also compromises the superdiffusive motion of beads in migrating amoebae [26]. Taken together, it is currently neither clear (i) which mechanism regulates the value of the anomaly exponent α in the cytoplasm nor (ii) how one should picture the emergence of heterogeneous subdiffu-

*Corresponding authors: diego.krapf@colostate.edu, matthias.weiss@uni-bayreuth.de

sion due to non-specific interactions in an actively driven environment.

Here, we address these points by extensive SPT experiments on individual quantum dots loaded into the cytoplasm of living mammalian cells. In particular, we quantify the particles' motion in the cytoplasm of untreated cells and in cells where the actin or microtubule cytoskeleton has been disrupted. Upon breaking down microtubules, a significant change towards more subdiffusive motion is observed. By comparing our experimental data to the dynamics of organelles, we arrive to the conclusion that non-specific binding of tracers to the vast ER network is responsible for the emergence of a marked cytoplasmic subdiffusion. The ER is further responsible for coupling the dynamics of cytoplasmic particles to active microtubule-based processes. Our experimental data are well described by an intermittent FBM model that switches stochastically between a higher or lower mobility while moving in the aqueous cytosol or on segments of the ER network, enforcing a heterogeneous FBM-like transport of tracers that is characteristic of the cytoplasmic subdiffusion in eukaryotic cells.

To explore the heterogeneous subdiffusion in the cytoplasm of mammalian cells, we performed extensive SPT on quantum dots that had been introduced into the cytoplasm of cultured HeLa cells by bead loading [33, 34]. Measurements were performed with a sampling time of $\Delta t = 100$ ms, and quantum dot trajectories were first evaluated in terms of their time-averaged MSD (TA-MSD) using $N = 100$ or $N = 500$ positions,

$$\langle r^2(\tau)\rangle_t = \frac{1}{N-k}\sum_{i=1}^{N-k}\left[\mathbf{r}((i+k)\Delta t) - \mathbf{r}(i\Delta t)\right]^2 \quad . \qquad (1)$$

Following previous reports [18, 35, 36], individual TA-MSDs were fitted with a simple power law $\langle r^2(\tau)\rangle_t = K_\alpha \tau^\alpha$ in the range $\Delta t \le \tau \le 10\Delta t$ to extract the anomaly exponent α and the generalized diffusion coefficient K_α. The resulting probability density function (PDF) of anomaly exponents, $p(\alpha)$, showed considerable trajectory-to-trajectory fluctuations around a mean $\langle\alpha\rangle \approx 0.57$ (Fig. 1a and Fig. S1a [34]) that slightly depends on the trajectory length N (Table I).

To probe a potential perturbation of the power-law scaling due to static and dynamic localization errors [37], and to validate the significance of the mean exponent $\langle\alpha\rangle$, we exploited a bootstrapping approach: From the whole set of calculated TA-MSDs we drew randomly a non-exhaustive ensemble of 100 curves, averaged these geometrically, and used again a simple power-law fit to extract the scaling exponent α of the resulting ensemble-averaged TA-MSD (see [34] for details). Repeating this approach $M = 200$ times, we noted that none of the ensemble-averaged TA-MSDs showed a significant offset in the extrapolated limit $t \to 0$ (Fig. S2 [34]), i.e. static and dynamic localization errors appear to cancel each other in our data and therefore fitting with a simple power law gives meaningful results for α.

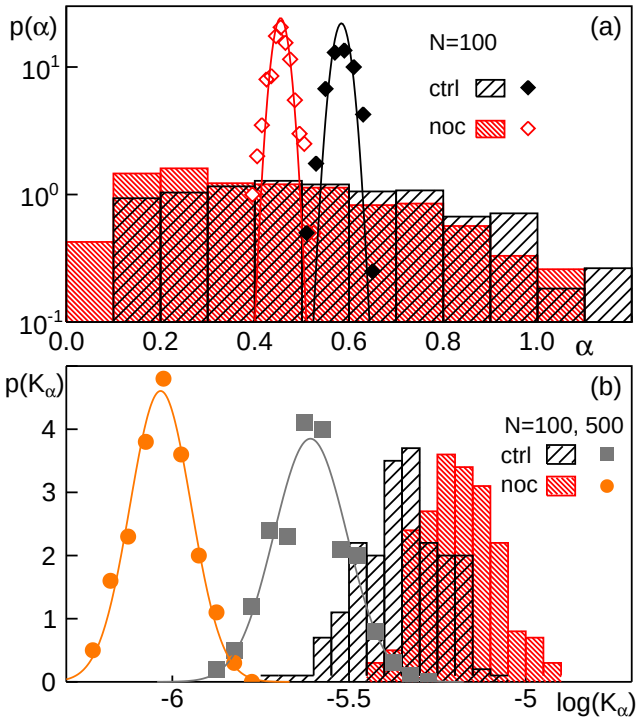

FIG. 1: (a) The PDF of anomaly exponents α, obtained from individual TA-MSDs ($N = 100$), shows a broad variation around a mean $\langle\alpha\rangle = 0.59$ in untreated cells (black histogram). Nocodazole-treated cells have a similarly broad PDF (red histogram) with a significantly lower mean (cf. Table I). Similar results are found for longer trajectories ($N = 500$, Fig. S1a [34]). Using a bootstrapping approach with geometric averaging (diamonds with full lines being Gaussian fits) resulted in narrower PDFs with the same mean anomaly exponent. (b) PDFs of the generalized transport coefficient K_α, obtained by the bootstrapping method, roughly have a lognormal shape (full lines) in untreated and nocodazole-treated cells. Short trajectories ($N = 100$, histograms with color-coding as before) exhibit a small change upon disrupting microtubules whereas longer trajectories ($N = 500$) appear more sensitive to treatment with nocodazole (squares and circles). Supposedly, a low K_α facilitates the acquisition of longer trajectories, biasing the data for $N = 500$.

The PDF of α values obtained with the bootstrapping approach (Fig. 1a) was very narrow with a mean $\langle\alpha\rangle$ that matched the respective value found before via individual TA-MSDs (Table I). Geometric averaging of TA-MSDs boils down to an arithmetic averaging of individual α values (but not of K_α). Thus, the narrow width of $p(\alpha)$ after bootstrapping is determined by $\sigma/\sqrt{M}$, where σ is the standard deviation of α derived from individual TA-MSDs. An arithmetic instead of a geometric averaging of TA-MSDs leads to an overestimation of the mean scaling exponent (Table I and Fig. S1b [34]).

Being interested in how cytoplasmic diffusion is affected by the cytoskeleton, we applied either nocodazole to break down microtubules, or cytochalasin D or

	control	noc	cyto D	lat A
TA-MSDs	0.59 (0.55)	0.46 (0.36)	0.58 (0.54)	0.62 (0.58)
b.tr. geom.	0.58 (0.55)	0.46 (0.36)	0.58 (0.54)	0.61 (0.57)
b.tr. arith.	0.79 (0.60)	0.66 (0.43)	0.82 (0.73)	0.86 (0.76)

TABLE I: Mean anomaly exponents $\langle\alpha\rangle$ for trajectories of length $N = 100$ ($N = 500$) without treatment and after application of nocodazole, cytochalasin D, or latrunculin A (named control and noc, cyto D, or lat A, respectively). Standard errors were in all cases smaller than 0.02.

latrunculin A to disrupt actin filaments. Disrupting microtubules changed the diffusion anomaly substantially (Fig. 1a and Table I) whereas disrupting actin networks had no significant effect (Table I). Transport coefficients K_α showed a higher sensitivity to microtubule disruption and also a stronger dependence on trajectory length (Fig. 1b). Similar to previous observations on the dynamics of the ER [32], the effect of nocodazole on K_α was not particularly strong for short trajectories. For longer trajectories ($N = 500$), however, a marked shift to smaller transport coefficients was visible upon microtubule disruption. This puts up a caveat that longer trajectories may represent a distinct subset of the acquired data, e.g. a lower mobility facilitating the tracking, but it also indicates that microtubule-associated processes significantly contribute to the diffusion anomaly in untreated cells beyond a change in the scaling of MSDs.

Going beyond the MSD, we analyzed the ensemble average of the velocity autocorrelation function (VACF),

$$C_v(\tau) = \langle \mathbf{v}(t)\mathbf{v}(t+\tau)\rangle_{t,E} \qquad (2)$$

that is highly sensitive to the nature of unconfined anomalous diffusion processes [38, 39]. Here, $\mathbf{v}(t) = [\mathbf{r}(t+\delta t) - \mathbf{r}(t)]/\delta t$ is the velocity at time t, given via the increments in a period δt. Varying $\delta t = k\Delta t$ in multiples of the sampling time Δt, the VACFs showed in all cases a pronounced negative peak for $\tau = \delta t$ as expected for antipersistent random walks. By rescaling the times as $\xi = \tau/\delta t$, all VACF traces collapse to a single master curve that agrees with the analytical predictions for FBM (Fig. 2 and Fig. S3a [34]), namely

$$C_v(\xi) = \frac{(\xi+1)^\alpha + |\xi-1|^\alpha - 2\xi^\alpha}{2}\,, \qquad (3)$$

with α being set to the value $\langle\alpha\rangle$ found with the bootstrapping protocol (Table I). We emphasize the exceptional agreement of the experimental data with Eq. (3) without any fitting parameters since other antipersistent random walk data, e.g. from membrane proteins, can deviate significantly from the FBM prediction (see Fig. S3b [34] for an example).

Next we inspected the PDF of the normalized increments $\chi_{\delta t}$ within a time lag δt [25]. The time series $\Delta x_i = x_{i+k} - x_i$ and $\Delta y_i = y_{i+k} - y_i$ were calculated and normalized by their mean step lengths $\langle|\Delta x_i|\rangle$ and $\langle|\Delta y_i|\rangle$

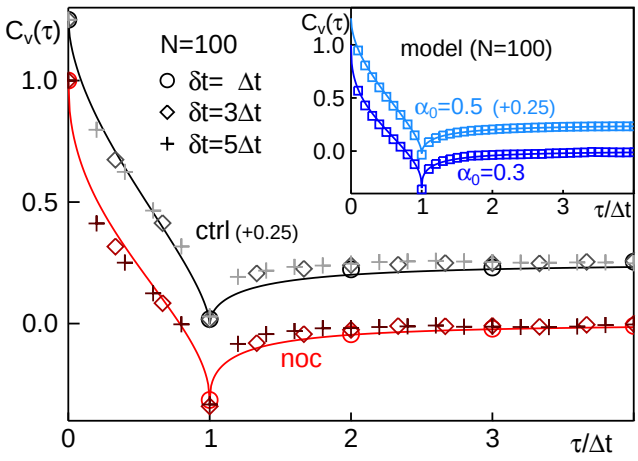

FIG. 2: The rescaled normalized VACF [Eq. (2)] of all experimental trajectories with $N = 100$ at different δt agrees with the predicted analytical form for FBM (full lines, Eq. (3)), both without treatment (grey symbols) and after nocodazole-treatment (red symbols). For better visibility, untreated cell data have been shifted upwards. No significant differences are seen for longer trajectories ($N = 500$, Fig. S3a [34]). Inset: VACFs of simulated intermittent FBM realizations with $N = 100$ and indicated anomaly values α_0 also agree with Eq. (3) full lines).

for each trajectory. Since no systematic differences were observed between x- and y-directions, all normalized increments were combined into a single set of $\chi_{\delta t}$. For a homogeneous FBM, a Gaussian PDF $p(\chi_{\delta t})$ is expected for all δt. Yet, for small δt our data showed significant deviations from a Gaussian in the tails of the distribution (Fig. 3). This suggests that individual trajectories are heterogeneous, i.e. the particle mobility changes within the trajectory. For $\delta t = 10\Delta t$, this heterogeneity subsides, collapsing the increment statistics to the anticipated Gaussian (Fig. S4 [34]).

Based on the observation of a heterogeneous and cytoskeleton-dependent subdiffusion of quantum dots in the cytoplasm, we hypothesized that an intermittent FBM model can correctly describe the data. Moreover, the similarities of $\langle\alpha\rangle$ in Table I with previously reported data for ER structures [32] triggered the idea that quantum dots transiently associate with the ER network between periods of exploring the surrounding aqueous cytosol. We therefore modeled the dynamics of individual particles as FBM with fixed anomaly α_0 and a transport coefficient that randomly switches within each trajectory (see [34] for technical details). Particles were assumed to exist in 'on' and 'off' states with coefficients $K_\alpha^{\rm on} < K_\alpha^{\rm off}$, representing ER-associated and free motion. Dichotomous switching between these states was modeled as a Markov process with transition rates $k_{\rm on}$ and $k_{\rm off}$. In our simulations we kept these rates and the ratio $s = K_\alpha^{\rm on}/K_\alpha^{\rm off}$ fixed, and chose $\alpha_0 = 0.5$ ($\alpha_0 = 0.3$) for untreated (nocodazole-treated) cells, in accordance

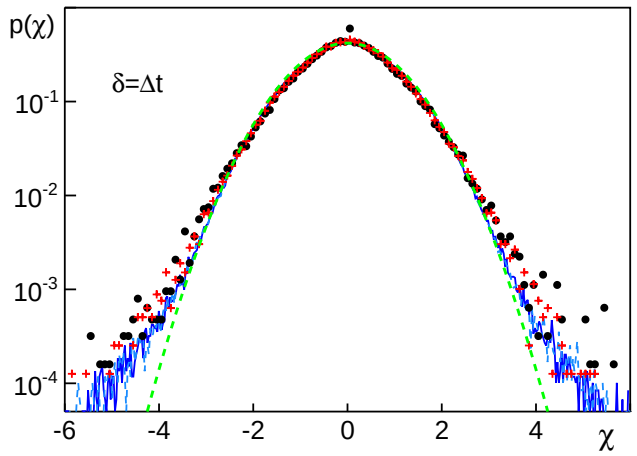

FIG. 3: The PDF of normalized increments $\chi_{\delta t}$ from trajectories with $N = 100$ for a time lag $\delta t = \Delta t$ follows Gaussian (green dashed line) for small χ but shows significant deviations at large χ, suggesting a heterogeneous random walk process (black circles and red crosses: untreated and nocodazole-treated, respectively). The data are in good agreement with simulations of an intermittent FBM model ($\alpha_0 = 0.5$ and $\alpha_0 = 0.3$: coinciding light and dark blue lines). For $\delta t = 10\Delta t$, experimental data and simulations follow a Gaussian for all χ (cf. Fig. S4 [34]).

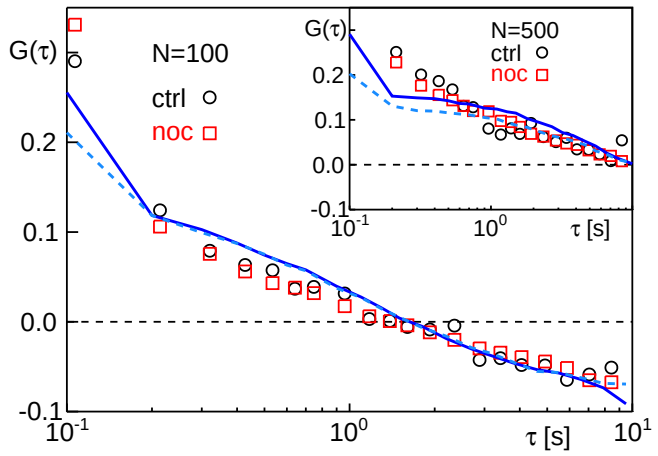

FIG. 4: The autocorrelation function of fluctuations in the squared increments, $G(\tau)$, of short trajectories ($N = 100$) shows a non-trivial decay for untreated and nocodazole-treated cells (black and red symbols, respectively), indicating a temporal change of transport parameters. These data are in very good agreement with simulation results of an intermittent FBM model (light and dark blue lines). Inset: Also for longer trajectories ($N = 500$), a non-trivial decay of $G(\tau)$ is observed that is well matched by simulation results of an intermittent FBM model.

with the previously reported anomaly values for ER junctions [32]. Despite the simplicity of this model, we observed a surprisingly good overlap with our experimental data for $s = 3.5$, $k_{\text{on}} \approx 0.27\ \text{s}^{-1}$, and $k_{\text{off}} \approx 0.01\ \text{s}^{-1}$: First, the mean anomaly of simulated realizations, extracted from TA-MSDs, was $\langle\alpha\rangle \approx 0.55$ and $\langle\alpha\rangle \approx 0.37$, respectively, in agreement with the experimental observations (Table I). The slightly larger value as compared to the imposed value α_0 is a consequence of the dichotomous switching that perturbs the pure FBM behavior. Second, when using the respective value $\langle\alpha\rangle$, the VACF showed the same agreement with Eq. (3) as the experimental data (insets of Fig. 2 and Fig. S3a). Third, the non-Gaussian shape of the increment statistics $\chi_{\delta t}$ for $\delta t = \Delta t$ and the more Gaussian shape for $\delta t = 10\Delta t$ are almost perfectly matched (Fig. 3 and Fig. S4 [34]). Hence, a switching between just two states is sufficient for reproducing key features of our data.

The dichotomous process predicts that the ensemble-averaged autocorrelation function of fluctuations in the squared increments $\Delta r^2(t) = |\mathbf{r}(t + \Delta t) - \mathbf{r}(t)|^2$, defined as

$$G(\tau) = \left\langle \frac{\langle \Delta r^2(t) \cdot \Delta r^2(t+\tau)\rangle_t - \langle \Delta r^2(t)\rangle_t^2}{\langle \Delta r^2(t)\rangle_t^2} \right\rangle_E , \quad (4)$$

should show a characteristic long-lasting decay that depends only on the dwell times in the two states. Essentially, $G(\tau)$ describes how long a random walk is fueled by a homogenous PDF of steps with a given mean length before switching to a different mean step length. For pure FBM trajectories, $G(\tau) = 0$ for $\tau > \Delta t$ (Fig. S5 [34]) whereas the intermittent model yields $G(\tau) \sim \exp[-(k_{\text{on}} + k_{\text{off}})\tau]$ for sufficiently long trajectories [40]. For small N, however, the fairly slow switching is not sampled well within each trajectory, leading to strongly fluctuating asymptotic zero lines that are eventually ensemble-averaged. As a result, a long-lasting decay emerges that appears to be unbounded. This prediction of the intermittent FBM model also agrees surprisingly well with the behavior of the experimental data (Fig. 4).

To probe more directly the apparent mobility switching within individual trajectories, we employed a recently developed analysis based on a trajectory's local convex hull [41] (see [34] for details). This analysis confirmed the existence of at least two mobility states (Fig. S6a) and indicated a markedly larger mean residence time in the low-mobility state (Fig. S6b) for untreated and nocodazole-treated cells with an apparently Markovian switching between these two states. Moreover, the obtained PDFs for the residence times of experimental trajectories were in favorable agreement with results obtained from trajectories of the intermittent FBM model, giving further support to the validity of the model.

What do our results imply and how can they be interpreted? Our experimental data are well described by an intermittent FBM model in which we have set $\alpha_0 = 0.5$ for untreated cells and $\alpha_0 = 0.3$ in the nocodazole-treated case. The same anomaly values have been observed experimentally for the motion of ER nodes in (un)treated

cells [32], suggesting that interactions with the ER are the dominant cause of a marked subdiffusion in cytoplasm. Transient association with the ER hampers free diffusion but also couples the particle motion to active microtubule-based processes. As a result, microtubule-mediated active noise leads to enhanced fluctuations in the motion of tracer particles transiently bound to the ER network, without binding of the particles to microtubules. The resulting diffusion heterogeneity does not require a full and elaborate model but rather a switching between two modes of motion (ER-associated and free) is sufficient to reproduce the experimental results. Overall, subdiffusion in the cytoplasm is indeed a considerably more complex phenomenon than anomalous diffusion in artificial fluids crowded with passive macromolecules.

Acknowledgments

We thank Mike Tamkun for discussions on experimental design, O'Neil Wiggan for providing HeLa cells, and Ashok Prasad and Wenlong Xu for providing the bead loader assembly and helping with the bead loading protocol. This work was financially supported by the German Academic Exchange Service (PPP USA grant No. 57315749). AS and MW also gratefully acknowledge financial support by the VolkswagenStiftung (Az. 92738).

[1] A. B. Fulton, Cell **30**, 345 (1982).
[2] R. Ellis, Trends Biochem. Sci. **26**, 597 (2001).
[3] F. Höfling and T. Franosch, Rep. Prog. Phys. **76**, 046602 (2013).
[4] M. Weiss, Int. Rev. Cell Mol. Biol. **307**, 383 (2014).
[5] K. Norregaard, R. Metzler, C. M. Ritter, K. Berg-Sørensen, and L. B. Oddershede, Chem. Rev. **117**, 4342 (2017).
[6] E. Kepten, I. Bronshtein, and Y. Garini, Phys. Rev. E **83**, 041919 (2011).
[7] M. Magdziarz and A. Weron, Phys. Rev. E **84**, 051138 (2011).
[8] R. Metzler, J.-H. Jeon, A. G. Cherstvy, and E. Barkai, Phys. Chem. Chem. Phys. **16**, 24128 (2014).
[9] B. B. Mandelbrot and J. W. Van Ness, SIAM Rev. **10**, 422 (1968).
[10] G. Guigas, C. Kalla, and M. Weiss, Biophys. J. **93**, 316 (2007).
[11] J. Szymanski and M. Weiss, Phys. Rev. Lett. **103**, 038102 (2009).
[12] S. C. Weber, A. J. Spakowitz, and J. A. Theriot, Phys. Rev. Lett. **104**, 238102 (2010).
[13] I. M. Sokolov, Soft Matter **8**, 9043 (2012).
[14] D. Ernst, M. Hellmann, J. Köhler, and M. Weiss, Soft Matt. **8**, 4886 (2012).
[15] D. Krapf, in *Curr. Top. Membr.* (Elsevier, 2015), vol. 75, pp. 167–207.
[16] M. Weiss, M. Elsner, F. Kartberg, and T. Nilsson, Biophys. J. **87**, 3518 (2004).
[17] D. S. Banks and C. Fradin, Biophys. J. **89**, 2960 (2005).
[18] F. Etoc, E. Balloul, C. Vicario, D. Normanno, D. Lisse, A. Sittner, J. Piehler, M. Dahan, and M. Coppey, Nat. Mater. **17**, 740 (2018).
[19] I. Wong, M. Gardel, D. Reichman, E. R. Weeks, M. Valentine, A. Bausch, and D. A. Weitz, Phys. Rev. Lett. **92**, 178101 (2004).
[20] J. F. Nagle, Biophys. J. **63**, 366 (1992).
[21] M. J. Saxton, Biophys. J. **70**, 1250 (1996).
[22] S. K. Ghosh, A. G. Cherstvy, and R. Metzler, Phys. Chem. Chem. Phys. **17**, 1847 (2015).
[23] J. Nixon-Abell, C. J. Obara, A. V. Weigel, D. Li, W. R. Legant, C. S. Xu, H. A. Pasolli, K. Harvey, H. F. Hess, E. Betzig, et al., Science **354** (2016).
[24] B. Wang, J. Kuo, S. C. Bae, and S. Granick, Nat. Mater. **11**, 481 (2012).
[25] T. J. Lampo, S. Stylianidou, M. P. Backlund, P. A. Wiggins, and A. J. Spakowitz, Biophys J **112**, 532 (2017).
[26] P. Witzel, M. Gotz, Y. Lanoiselee, T. Franosch, D. S. Grebenkov, and D. Heinrich, Biophys J **117**, 203 (2019).
[27] A. G. Cherstvy, A. V. Chechkin, and R. Metzler, New J. Phys. **15**, 083039 (2013).
[28] M. V. Chubynsky and G. W. Slater, Phys. Rev. Lett. **113**, 098302 (2014).
[29] A. V. Chechkin, F. Seno, R. Metzler, and I. M. Sokolov, Phys. Rev. X **7**, 021002 (2017).
[30] A. G. Cherstvy and R. Metzler, Phys. Chem. Chem. Phys. **18**, 23840 (2016).
[31] L. Stadler and M. Weiss, New J. Phys. **19**, 113048 (2017).
[32] K. Speckner, L. Stadler, and M. Weiss, Phys. Rev. E **98**, 012406 (2018).
[33] P. L. McNeil and E. Warder, J. Cell Sci. **88**, 669 (1987).
[34] See Supplemental Material at [URL will be inserted by publisher] for methods details and supplemental figures.
[35] C. Manzo and M. F. Garcia-Parajo, Rep. Prog. Phys. **78**, 124601 (2015).
[36] A. Weron, K. Burnecki, E. J. Akin, L. Solé, M. Balcerek, M. M. Tamkun, and D. Krapf, Sci. Rep. **7**, 5404 (2017).
[37] M. P. Backlund, R. Joyner, and W. E. Moerner, Phys. Rev. E **91**, 062716 (2015).
[38] S. Burov, J.-H. Jeon, R. Metzler, and E. Barkai, Phys. Chem. Chem. Phys. **13**, 1800 (2011).
[39] S. C. Weber, M. A. Thompson, W. Moerner, A. J. Spakowitz, and J. A. Theriot, Biophys. J. **102**, 2443 (2012).
[40] J. Cao, Phys. Rev. E **63**, 041101 (2001).
[41] Y. Lanoiselee and D. S. Grebenkov, Phys. Rev. E **96**, 022144 (2017).

Elucidating the origin of heterogeneous anomalous diffusion in the cytoplasm of mammalian cells
– Supplementary Information –

Adal Sabri and Matthias Weiss
Experimental Physics I, University of Bayreuth, Universitätsstr. 30, D-95447 Bayreuth, Germany

Xinran Xu
Department of Electrical and Computer Engineering, Colorado State University, Fort Collins, CO 80523, USA

Diego Krapf
Department of Electrical and Computer Engineering, Colorado State University, Fort Collins, CO 80523, USA and School of Biomedical Engineering, Colorado State University, Fort Collins, CO 80523, USA

I. MATERIALS AND METHODS

A. Cell culture

HeLa (human cervical cancer) cells were cultured in Dulbecco's Minimal Essential Medium (DMEM; Invitrogen,Carlsbad, CA) with phenol red, supplemented with 10% fetal calf serum (FCS; Biochrom, Holliston, MA) and 1% penicillin/streptavidin (ThermoFisher, Gibco, Waltham, MA) and incubated in Corning tissue-culture treated culture dishes at 37°C in a 5% CO_2 atmosphere. For imaging, cells were plated on 35 mm diameter ΔT dishes (Bioptech, Butler, PA) with ITO coating for temperature control. Prior to plating, the dishes were coated with 0.5% matrigel matrix ($c_{\mathrm{protein}} = 8 - 12$ mg/ml; Corning Life Sciences, NY) in Opti-MEM (ThermoFisher, Gibco, Waltham, MA). Experiments were performed 36-48 h after seeding.

Microtubule depolymerization was performed on the day of the experiment using nocodazole as described before [1–3]. Prior to microtubule breakdown, tracer particles (Qdot 655 ITK Carboxyl core (CdSe)-shell (ZnS), ThermoFisher, Waltham, MA) provided as 8 μM solution in 50 mM borate, pH 9.0 (working concentration 1:1000 in PBS with 1% BSA) were incorporated to the cytoplasm by the bead-loading technique [4] using 100 μm diameter glass beads (G4649-100G, Sigma Aldrich, St. Louis, MO). After bead loading, cells were incubated for another 45 min at 37°C. Glass beads were washed off gently with PBS and DMEM without phenol red, supplemented with 0.1% nocodazole ($c_{\mathrm{stock}} = 10$ mM in DMSO) and 0.1% Hoechst 33342 (10 mg/ml; Invitrogen, Carlsbad, CA) was added for staining the chromatin. The dish was stored on ice for 10 min prior to 15 min recovery at 37°C in a 5% CO_2 atmosphere before performing the experiments.

Depolymerization of actin filaments was achieved using latrunculin A or cytocalasin D, respectively. On the day of the experiment, cells were loaded with quantum dots as described before and recovered for 45 min at 37°C. Glass beads were washed gently with PBS and cells were incubated in DMEM without phenol red, supplemented with 200 nM latrunculin A or 2 μM cytocalasin D, and 0.1% Hoechst 33342 for another 30 min at 37°C prior to the experiments.

B. Imaging

Images were acquired using Nikon NIS-Elements 4.51 software in a custom-built microscope equipped with an Olympus PlanApo 100× NA1.45 objective and a CRISP ASI autofocus system [5]. Optical aberrations of the imaging system were corrected using a MicAO 3DSR adaptive optics system (Imagine Optic, Orsay, France) inserted into the emission pathway between the microscope and the EMCCD camera [6]. The sample temperature was kept at 37°C using a Bioptechs stage heater. Quantum dots were excited with a 561-nm laser (OBIS 561nm LS 100mW, Coherent, Santa Clara, CA) under continuous illumination. For excitation, an optical density filter with ND=1 was used and an incident angle below the critical angle was chosen to provide a penetration depth of multiple micrometers. Emission was collected through the appropriate Semrock bandpass filters and images were acquired in a water-cooled, back-illuminated EMCCD camera (iXon DU-888, Andor, Belfast, UK) operated at −85°C at a rate of 10 frames/s over a total period of 2000 frames. Fluorescent images of the Hoechst-stained chromatin were acquired using a 405 nm laser (SDL-405-LM-050, Shanghai Dream Lasers, Shanghai, China) prior to and right after the quantum dots sequences with an exposure time of ~ 110 ms. Bright field images of the cells were also acquired prior to and after imaging.

C. Single particle tracking and trajectory analysis

Trajectories were extracted from image stacks with FIJI/TrackMate [7]. As an input for TrackMate, the blob diameter of Qdots was estimated via the intensity profiles of 30 quantum dots immobilized on a coverslip, yielding an average FWHM of the point-spread function of 3.2 ± 0.5 pixels. Tracking was performed using the Laplacian-of-Gaussian algorithm (blob diameter set to 4 pixels, threshold set to 200, median filter and sub-pixel localization switched on). No additional filters were applied to the detected spots. Identified particle positions were linked using the *simple LAP (linear assignment problem)* tracker adopted from Ref. [8]. A maximum linking distance of 2 pixels, a gap-closing maximum distance of 2 pixels, and a gap closing maximum frame gap of 2 were used. Subsequently the minimum number of spots in a track was set to $N \geq 50$ and the number of gaps was set to $n_g \leq 5$. The spot statistics and the tracks were extracted and exported as CSV and XML files, respectively. Tracks were converted to ASCII files in Matlab for subsequent processing and handling. Statistical analyses of trajectories (N positions with time lag Δt between successive frames) were performed in Matlab with custom-written codes that have been checked for proper function via FBM simulation data. Trajectories whose TA-MSD grew less than $\sim \tau^{0.075}$ were rated as immobile and were hence discarded from subsequent analyses. In total, $n = 83$, 57, 49, 75 cells (untreated or with nocodazole, cytochalasin D, latrunculin A, respectively) were used from which 4887, 9298, 2968, 3997 trajectories with $N = 100$ positions and 631, 841, 444, 517 trajectories with $N = 500$ positions were extracted. PDF bin sizes have been chosen according to Scott's rule throughout the manuscript.

As a control, we tracked quantum dots in cells treated with pure DMSO solvent without nocodazole, cytochalasin, or latrunculin. From five cells with 228 trajectories ($N = 100$) we obtained a mean anomaly $\langle\alpha\rangle = 0.65$ which is insignificantly higher than the value found for untreated cells. If DMSO has any effect, then it is rather a slight increase in $\langle\alpha\rangle$ whereas nocodazole led to a significantly smaller value. We therefore conclude that our results are not an artifact of DMSO.

D. Bootstrapping and averaging

Bootstrapping was performed by randomly selecting $n = 100$ trajectories and geometrically averaging their TA-MSDs, i.e. for each trajectory i the TA-MSD $\langle r^2(\tau)\rangle_t^{(i)}$ entered the geometric average as

$$\langle r^2(\tau)\rangle_{t,g} = \left(\prod_{i=1}^{n} \langle r^2(\tau)\rangle_t^{(i)}\right)^{1/n}. \tag{1}$$

Alternatively, the usual arithmetic average of the TA-MSDs, $\langle r^2(\tau)\rangle_t^{(i)}$ with $i = 1, \ldots, n$, was employed. We would like to note here that the logarithmic of Eq. (1) is similar to the mean-log-square displacement proposed by Kepten et al. [9] to reduce systematic errors in the estimation of $\langle\alpha\rangle$,

$$\log\left[\left(\prod_{i=1}^{n} \langle r^2(\tau)\rangle_t^{(i)}\right)^{1/n}\right] = \frac{1}{n}\sum_{i=1}^{n} \log\langle r^2(\tau)\rangle_t^{(i)}. \tag{2}$$

E. Local convex hull analysis

In order to directly visualize changes in the mobility within single trajectories, we employed the local convex hull (LCH) [10]. The integral-like character of this approach requires less statistics within the trajectories as compared to a local TA-MSD analysis that has proven useful for dissecting diffusive and ballistic motion [11]. For consistency with the PDF of normalized increments, $p(\chi_{\delta t})$, we rescaled all trajectories with $N = 100$ by their respective average displacement at the minimal length scale $\Delta r = \sqrt{\langle|x_{i+1} - x_i|\rangle^2 + \langle|y_{i+1} - y_i|\rangle^2}$ ($i = 1, \ldots, N-1$), and calculated then for each trajectory for all positions $i = 2, \ldots, N-2$ the largest diameter $S_d(t = i\Delta t)$ of the local convex hull of trajectory points $i-2, \ldots, i+2$. Assuming stationarity and hence combining all values for S_d of all trajectories from untreated cells into a single PDF revealed a non-Gaussian shape for $p(S_d)$ that suggests at least two states to be encoded in the trajectories (Fig. S6a). No significant difference was observed for trajectories from nocodazole-treated cells (see Fig. S6a).

In order to dissect the state with low mobility ('on') from all other states with a higher mobility ('off'), we fitted a Gaussian with mean μ and standard deviation σ to $p(S_d)$ in the range $S_d < \langle S_d\rangle$ (cf. Fig. S6a). Calculating the area under this Gaussian indicated that 85% of all S_d values come from trajectory segments with a low mobility, i.e. with

low S_d values. The remaining part of the PDF is due to at least one more state with a higher mobility that gives rise to larger S_d values. Assuming only two states, as in the intermittent FBM model, the ratio of weights for the low- and high-mobility pools suggests a ratio $k_{\rm on}/k_{\rm off} \approx 7$ for the mutual switching rates for untreated and nocodazole-treated cells.

Based on the described dissection of $p(S_d)$ into a low- and a high-mobility pool, we extracted residence times τ in the 'on' and 'off' states from individual trajectories ($N = 100$). To this end, we classified each value of a trajectory's time series $S_d(t)$ to be in the 'on'-state if $S_d(t) \leq \mu + 3\sigma$ and to be in the 'off'-state otherwise. The resulting PDF of residence times for untreated and nocodazole-treated cells are shown in Fig. S6b. Neglecting the peak at a residence time $\tau = N\Delta t$, i.e. omitting residence times that were cut by the finite length N of the time series, $p(\tau)$ showed an exponential PDF with mean residence times $\langle\tau_{\rm on}\rangle \approx 22\Delta t$ and $\langle\tau_{\rm off}\rangle \approx 3\Delta t$. The emergence of an exponential shape of $p(\tau)$ supports the assumption that switching between the low- and high-mobility state ('on' and 'off', respectively) is a Markovian process. Moreover, the ratio $\langle\tau_{\rm on}\rangle/\langle\tau_{\rm off}\rangle \approx 7$ is in agreement with the ratio $k_{\rm on}/k_{\rm off} \approx 7$ derived from $p(S_d)$ above.

It is worth noting at this point that the fairly short time series with only $N = 100$ positions certainly cannot accurately reveal the value of mean residence times if these are larger than $N\Delta t$. Yet, due to the Markovian nature of the switching process, one can obtain meaningful exponential PDFs of residence times that yield a significant estimate for the ratio $\langle\tau_{\rm on}\rangle/\langle\tau_{\rm off}\rangle$. In fact, applying the very same analysis to trajectories from simulations of the intermittent FBM model (see below for details) also revealed exponential PDFs for $p(\tau)$ with mean values $\langle\tau_{\rm on}\rangle \approx 16.5\Delta t$ and $\langle\tau_{\rm off}\rangle \approx 1.5\Delta t$ which is in favorable agreement with the results obtained from our experimental data.

F. Simulations

To describe the experimental data, an intermittent FBM model was constructed. First, two-dimensional FBM trajectories with a fixed diffusion anomaly α_0 were obtained via the Matlab routine *wfbm* with $i = 1, \ldots, N$ positions in each spatial dimension. From these trajectories $N - 1$ successive step increments (Δx, Δy) were extracted and re-scaled to yield a TA-MSD with transport coefficient $K_\alpha = 0.004\ \mu{\rm m/s}^\alpha$, which is in the range of experimentally observed values. For compatibility with experiments, the time increment between successive positions was chosen to be $\Delta t = 100$ ms. To arrive at a heterogeneous, i.e. intermittent, FBM random walk in a second step, a stochastic switching between two modes of motion with rates $k_{\rm on}$ and $k_{\rm off}$ was implemented: While the previously obtained random walk steps were left unchanged in the 'on'-state, all steps in the 'off'-state were multiplied by a factor $s > 1$ to model an enhanced mobility. As a result, the transport coefficient of the FBM trajectory switched randomly from K_α to sK_α (or back) with rate $k_{\rm off}$ and $k_{\rm on}$, respectively. Due to this perturbation, the TA-MSD of the tracjectories showed a scaling with a slightly larger exponent $\langle\alpha\rangle$ than the value α_0 imposed in the routine *wfbm*.

A very good matching to our experimental data with $N = 100$ positions (using an ensemble of 10^4 trajectories) was observed for $s = 3.5$, $k_{\rm on} = 0.27$/s, and $k_{\rm off} = 0.0096$/s with $\alpha_0 = 0.5$ for untreated cells and $\alpha_0 = 0.3$ after depolymerizing microtubules. For $N = 500$, the rates $k_{\rm on}$ and $k_{\rm off}$ both needed to be chosen sixfold lower to match the experimental observations, indicating that trajectories with this length are a distinct subset of the entire data set.

II. SUPPLEMENTARY FIGURES

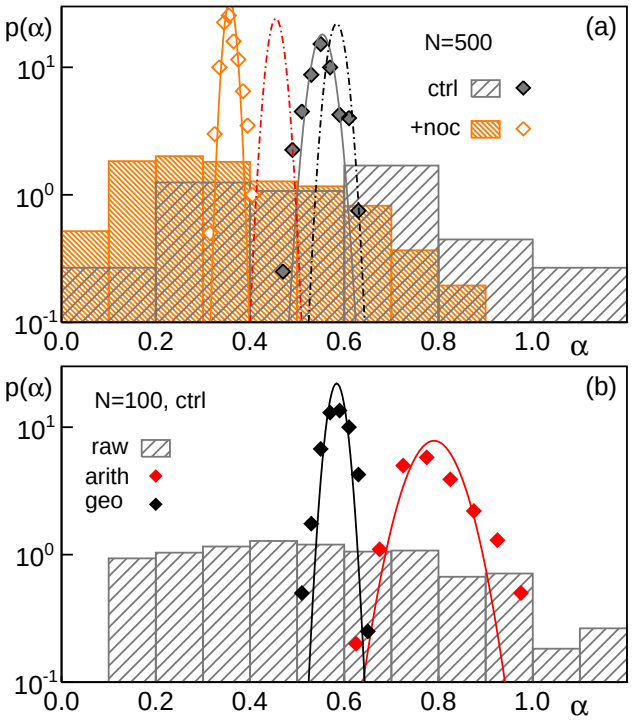

Figure S1: (a) In line with data shown in Fig. 1a in the main text, the PDF of anomaly exponents, $p(\alpha)$, as obtained from power-law fits on individual TA-MSDs of longer trajectories ($N = 500$) shows a fairly broad variation around a mean $\langle\alpha\rangle = 0.55$ in untreated cells (grey histogram). Nocodazole-treated cells have a similarly broad PDF (orange histogram) but feature a significantly lower mean (cf. Table I in the main text). Using the bootstrapping approach with geometric averaging (colored diamonds, full lines being best Gaussian fits) resulted in more narrow PDFs with the same mean anomaly. For better comparison with Fig. 1a, Gaussian fits to the bootstrapping data for $N = 100$ in untreated and nocodazole-treated cells are reproduced as black and red dash-dotted lines, respectively. (b) For the representative case of short trajectories ($N = 100$) in untreated cells, PDFs $p(\alpha)$ obtained from raw TA-MSD fitting (hatched histogram) and bootstrapping with geometric or arithmetic averaging (black and red diamonds, respectively) highlight a consistent over-estimation of the mean $\langle\alpha\rangle$ when using an arithmetic averaging (cf. also Table I in the main text). Full lines are best Gaussian fits to the bootstrapping data.

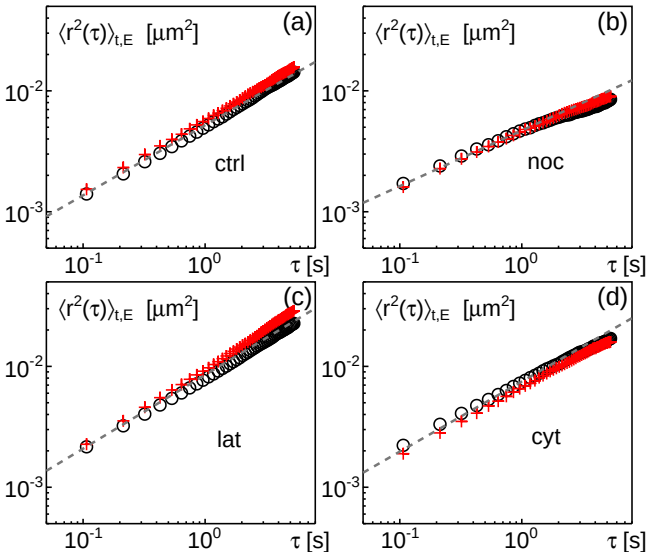

Figure S2: Representative geometrically averaged TA-MSDs (from trajectories with $N = 100$ positions) used for the bootstrapping approach (two examples, shown as black circles and red crosses) show no significant localization offsets at small lag times τ in (a) untreated, (b) nocodazole-, (c) latrunculin-, or (d) cytochalasin-treated cells. Grey dashed lines highlight the respective scaling given in Table I of the main text. This finding confirms and validates previously reported findings from comparable experiments [12] that had not been tested for perturbations by localization errors.

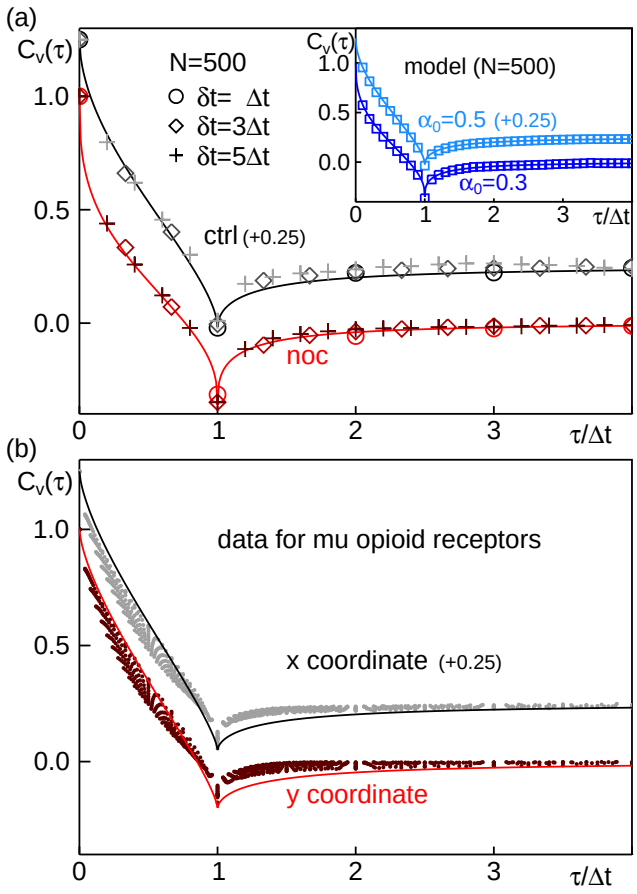

Figure S3: (a) The velocity autocorrelation function (VACF) for trajectories with $N = 500$ positions from untreated and nocodazole-treated cells agrees as well with the respective FBM prediction as the data for $N = 100$ (cf. Fig. 2 in the main text). Inset: The $N = 500$ trajectories for the intermittent FBM model also show a superb agreement with the prediction (full lines). (b) In contrast to quantum dots in the cytoplasm, the antipersistent motion of mu opioid receptors in the plasma membrane [13] show considerable deviations from the FBM prediction (full line).

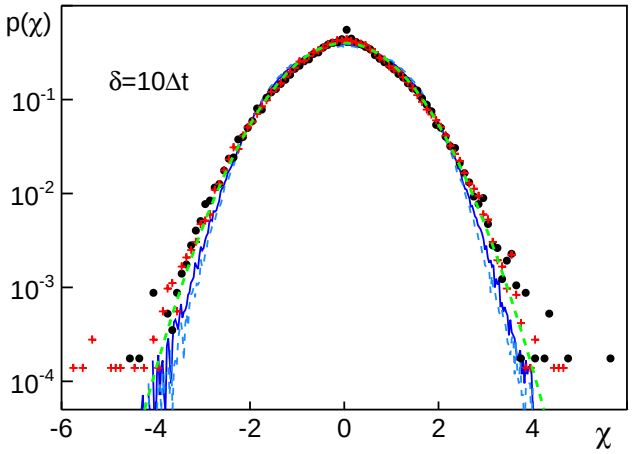

Figure S4: The PDF of normalized increments, $p(\chi)$, extracted from trajectories with $N = 100$ for a time lag $\delta t = 10\Delta t$, follows a Gaussian PDF (green dashed line) for all χ (black circles and red crosses: untreated and nocodazole-treated, respectively), i.e. deviations observed for $\delta t = \Delta t$ (Fig. 3, main text) have subsided. Also simulation data of an intermittent FBM model ($\alpha_0 = 0.5$ and $\alpha_0 = 0.3$: coninciding light and dark blue lines) are in good agreement with the Gaussian.

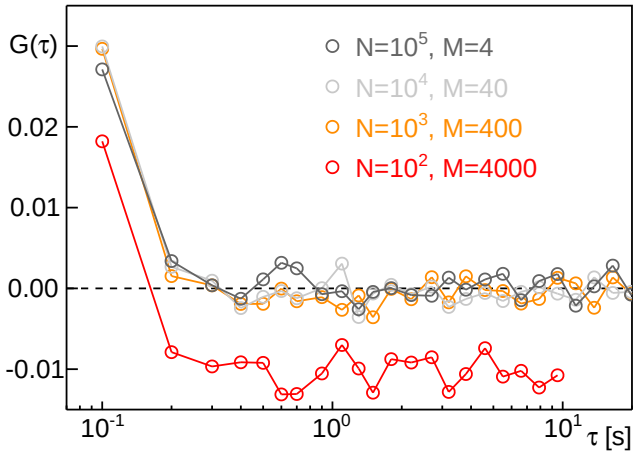

Figure S5: For an ensemble of M pure FBM trajectories with $\alpha = 0.7$ and N positions the autocorrelation function of squared increments, $G(\tau)$ is basically zero beyond the first point at the basic time increment, $\tau = \Delta t$. For short trajectories ($N = 100$, red circles), a constant negative value is assumed due to statistical errors: Subtracting the baseline when calculuating $G(\tau)$ is only correct up to an uncertainty $\sim 1/\sqrt{N}$, yielding a constant $G(\tau \gg \Delta t) \sim -1/N$ that subsides for longer trajectories.

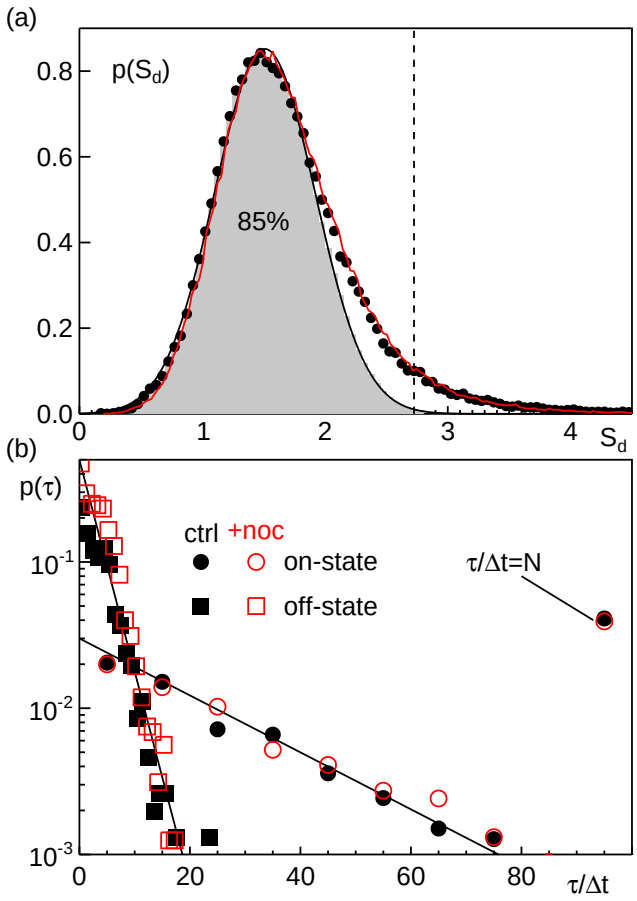

Figure S6: (a) The PDF $p(S_d)$ obtained from rescaled trajectories ($N = 100$) via the analysis of local convex hulls shows a marked peak that is well described by a Gaussian with mean $\mu = 1.5$ and standard deviation $\sigma = 0.4$ (full black line). No significant difference is seen between untreated cells (black symbols) and nocodazole-treated cells (full red line). Classifying the Gaussian's contribution to the PDF to represent a pool with low mobility ('on'-state) yields a weight of about 85% (grey area) whereas the tail in the PDF for larger S_d captures at least one state with higher mobility ('off'-state). The vertical dashed line indicates the value $\mu + 3\sigma$ used for dissecting individual trajectories into 'on'- and 'off'-states (see Methods for details). (b) The PDF of residence times in the 'on'- and 'off'-states (representing a low and high mobility state, respectively) have roughly an exponential shape (full black lines) with mean values $\langle \tau_{\mathrm{on}} \rangle \approx 22\Delta t$ and $\langle \tau_{\mathrm{off}} \rangle \approx 3\Delta t$, respectively. Residence times $\tau = N\Delta t$ (highlighted in the plot) have been omitted for obtaining mean residence times since they are bounded by the mere length of the time series. No significant difference is seen for untreated and noccodazole-treated cells.

[1] L. Stadler and M. Weiss, New J. Phys. **19**, 113048 (2017).
[2] K. Speckner, L. Stadler, and M. Weiss, Phys. Rev. E **98**, 012406 (2018).
[3] L. Stadler, K. Speckner, and M. Weiss, Biophys. J. **115**, 1552 (2018).
[4] P. L. McNeil and E. Warder, J. Cell Sci. **88**, 669 (1987).
[5] G. Campagnola, K. Nepal, B. W. Schroder, O. B. Peersen, and D. Krapf, Sci. Rep. **5**, 17721 (2015).
[6] M. G. Gervasi, X. Xu, B. Carbajal-Gonzalez, M. G. Buffone, P. E. Visconti, and D. Krapf, J. Cell Sci. **131**, jcs215897 (2018).
[7] J.-Y. Tinevez, N. Perry, J. Schindelin, G. M. Hoopes, G. D. Reynolds, E. Laplantine, S. Y. Bednarek, S. L. Shorte, and K. W. Eliceiri, Methods **115**, 80 (2017).
[8] K. Jaqaman, D. Loerke, M. Mettlen, H. Kuwata, S. Grinstein, S. L. Schmid, and G. Danuser, Nat. Meth. **5**, 695 (2008).
[9] E. Kepten, I. Bronshtein, and Y. Garini, Phys. Rev. E **87**, 052713 (2013).
[10] Y. Lanoiselee and D. S. Grebenkov, Phys. Rev. E **96**, 022144 (2017).
[11] D. Arcizet, B. Meier, E. Sackmann, J. O. Rädler, and D. Heinrich, Phys. Rev. Lett. **101**, 248103 (2008).
[12] F. Etoc, E. Balloul, C. Vicario, D. Normanno, D. Lisse, A. Sittner, J. Piehler, M. Dahan, and M. Coppey, Nat. Mater. **17**, 740 (2018).
[13] M. J. Metz, R. L. Pennock, D. Krapf, and S. T. Hentges, Sci Rep **9**, 7297 (2019).